Design and Optimization of a Bidirectional Dual Active Bridge DC-DC Converter using Dolphin Echolocation Algorithm for Microgrid Applications.

R Thushar Kumar Reddy

Department of Electrical and Electronics Engineering Vellore Institute of Technology Vellore-632014, India. rtkr2005@gmail.com

Abstract

The growing integration of renewable energy sources and energy storage technologies in modern microgrids necessitates the development of efficient bidirectional power conversion interfaces. This paper presents the design, mathematical modelling, and optimization of a Dual Active Bridge converter for microgrid applications using phase-shift modulation control. The converter facilitates efficient bidirectional power transfer between high and low voltage DC buses by establishing galvanic isolation using a high-frequency transformer. A complete state-space mathematical model captures the steady-state power flow properties as well as the transient dynamic behavior of the system. The proportional-integral controller parameters are optimized using the dolphin echolocation algorithm, a nature-inspired metaheuristic technique that mimics dolphin hunting strategies.

Keywords - Dual Active Bridge, Bidirectional Converter, Phase Shift Modulation, Dolphin Echolocation Algorithm, PI Controller Optimization, Microgrid, State-Space Modeling

Objective

The primary objectives of this research work are outlined as follows:

1. To provide a thorough mathematical model of the Dual Active Bridge bidirectional DC-DC converter that includes transient state-space representation, steady-state characteristics, and power flow equations for precise system analysis and control design.

2. To improve transient response and steady-state performance by using the dolphin echolocation algorithm to systematically optimize PI controller gains (Kp and Ki) by minimizing integral absolute error as the fitness function.

3. To verify the suggested design using extensive MATLAB Simulink simulations that examine power transfer characteristics, error signal dynamics, voltage regulation, and current waveforms under various operating conditions.

Comparative Table

S.No	Previous Work Literature	Innovation By Your Project
1	For DAB converters, conventional PI controller tuning techniques like Ziegler-Nichols or trial-and-error methods lack systematic optimization and frequently produce subpar performance with slower transient response.	Superior transient response and short settling time are achieved by using the dolphin echolocation algorithm, which offers systematic, automated optimization of controller gains through iterative fitness evaluation.
2	The converter behavior over broad operating ranges and parameter variations may not be accurately represented by conventional DAB control designs, which rely on Fourier-based analysis or simplified small-signal models.	Detailed state-space mathematical model development that captures both transient dynamics and steady-state power flow allows for thorough system analysis and accurate controller design under a range of operating conditions.
3	In the absence of a comprehensive optimization framework that blends mathematical precision with astute tuning algorithms, most existing works focus on modeling or control implementation separately.	Integrated strategy for controller parameter selection that combines exacting mathematical modeling with a bio-inspired optimization algorithm, verified by thorough Simulink implementation with real circuit-level simulation.

Introduction

A micro-grid is a local network that combines different energy resources and storage options, allowing it to operate independently or alongside the main utility grid. These networks often include a variety of sources like solar panels, wind turbines, fuel cells, and batteries.

It's a simple idea, but it makes day-to-day operation much smoother, maybe even more resilient during short peaks. Among isolated bidirectional designs, the Dual Active Bridge has drawn a lot of interest in research and in practice. In most cases, this leads to a cleaner design and reliable performance, which is why engineers tend to choose it for storage interfaces and similar tasks.

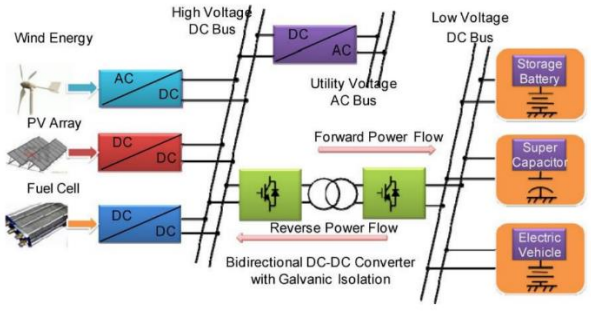

Figure 1: Layout of Bi-directional DC-DC Converter in Microgrid Applications

A high-frequency transformer sits between the input and output and keeps them electrically isolated, which improves safety. By choosing an appropriate turns ratio, it also lets you match voltages without much fuss. In many designs, the transformer's own leakage inductance does most of the work of moving energy from one side to the other, so you can often avoid adding large external inductors. That saves space and parts. DAB converters also stand out because they can run with soft switching-most often zero-voltage switching. This cuts the switching losses in the semiconductors, which matters more and more as power levels rise, when those losses might otherwise dominate and pulls down efficiency. Control is handled with phase-shift modulation: you set the power flow by shifting the phase between the primary and secondary bridge voltages. It is a simple method to implement, yet it tends to respond well and stay stable over a broad range of operating conditions.

Despite extensive research on DAB converter design and control, optimal tuning of feedback controller parameters remains a challenging task. Classical analytical methods such as root-locus, bode plot analysis, or empirical techniques like Ziegler-Nichols tuning often provide acceptable starting points but may fail to achieve optimal performance considering the complex nonlinear dynamics, parametric uncertainties, and varying operating conditions encountered in practical microgrid applications. Manual iterative tuning processes are time-consuming and highly dependent on designer experience, potentially leading to suboptimal compromises between competing performance objectives such as settling time, overshoot, and robustness.

Natural computing-based optimization methods were found to be very successful in solving complex engineering optimization problems by mimicking processes and behaviours that take place in natural systems. These techniques, known as meta-heuristics, are particularly good for searching in high dimensions (superior to an exhaustive search), exploring and exploiting while avoiding the convergence of a minimum. The dolphin echolocation optimization (DEO), as a new member of this algorithm family, is done based on how real dolphins use the biosonar and assemble advanced hunting techniques for living in their habitat.

Dolphins echolocate by releasing clicks or burst pulse sounds and then listening for the return echo to determine the place, size along with shape of objects. Even in low light or turbid waters with limited visual observations, this biological process reveals outstanding precision. This activity is summarized in the computational algorithm as an iterative way of searching, where a population of solution candidates are exploring parameter space and adjusting their position through fitness evaluations: however, it only moves guided by previously generated best solution.

Working of DAB Bi-Directional Converter

The transformer primary voltage, V1 and secondary voltage, V2 relate with the power transfer between ports of the DAB power converter which is shown in Fig. 1, as follows

$$P = \frac{V_1 V_2}{n\ w_s L_{eq}} \theta \left(1 - \frac{\theta}{\pi}\right) \qquad (1)$$

Where θ is the phase angle difference between voltages V_1 and V_2 , ω_s is the switching frequency of DAB is rad/sec, L_{eq} is the equivalent inductor of the power converter, and 1: n is the transformation ratio of the transformer. In this case, the high voltage port, V1 can be DC link of hybrid system say photovoltaic terminals and DC link of the grid tied inverter (e.g. 400V). The low voltage port V2 may be the energy storage: battery or ultracapacitor (48V).

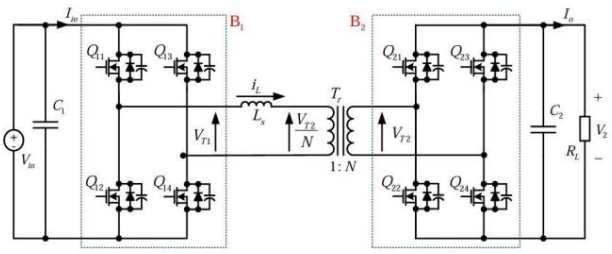

Figure 2: Schematic Diagram of Single Phase DAB Bi-directional Converter

A. Buck operation (Forward power transfer)

In buck operating mode, the power transfers from high voltage port V1 to the low voltage port V2. In this mode, generated gate pulses of the HV side leads the LV side by an angle θ, and power transfers from primary to secondary. Fig. below is showing the switching period of both bridges and current and voltage waveforms of the equivalent inductor. Table-I shows switching states of devices.

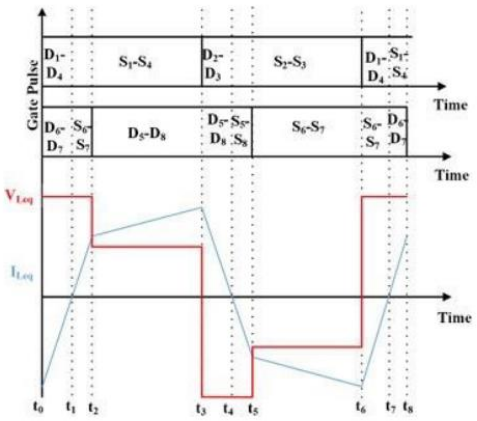

TABLE I
SWITCHING STATES OF CONVERTER IN BUCK MODE

Time duration	Switching States
$t_0 < t < t_1$	D_1-D_4 and D_6-D_7
$t_1 < t < t_2$	S_1-S_4 and S_6-S_7
$t_2 < t < t_3$	S_1-S_4 and D_5-D_8
$t_3 < t < t_4$	D_2-D_3 and D_5-D_8
$t_4 < t < t_5$	S_2-S_3 and S_5-S_8
$t_5 < t < t_6$	S_2-S_3 and S_6-S_7
$t_6 < t < t_7$	D_1-D_4 and D_6-D_7
$t_7 < t < t_8$	S_1-S_4 and S_6-S_7

B. Boost operation (Reverse power transfer):

In this mode, the battery starts discharging by supplying energy to the 400V input DC link which is a boost operation. In this case, generated gate pulses at the HV side VSC lags LV side by an angle θ, and power transfers from secondary to primary side. Switching states of devices are provided in Table-II. The current and voltage across equivalent inductor is shown in Fig. below, referring gate pulses of both bridges.

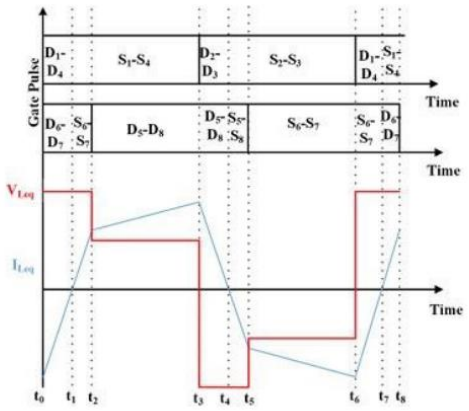

TABLE II
SWITCHING STATES OF CONVERTER IN BUCK MODE

Time duration	Switching States
$t_0 < t < t_1$	D_2-D_3 and S_6-S_7
$t_1 < t < t_2$	S_2-S_3 and D_6-D_7
$t_2 < t < t_3$	D_1-D_4 andD_6-D_7
$t_3 < t < t_4$	D_1-D_4 and S_5-S_8
$t_4 < t < t_5$	S_1-S_4 and D_5-D_8
$t_5 < t < t_6$	D_2-D_3 and D_5-D_8
$t_6 < t < t_7$	D_2-D_3 and S_6-S_7
$t_7 < t < t_8$	S_2-S_3 and D_6-D_7

Power Flow Equations

The average power transferred from the primary to secondary side under single-phase-shift modulation with 50% duty cycle operation can be derived through volt-second balance analysis across the series inductance. Fig. below is the voltage analysis graph at different time intervals. The fundamental relationship governing steady-state power transfer is expressed as:

$$0 < t < \emptyset: \qquad v_L = v_1 + \frac{v_2}{N}$$

$$0 < t < \frac{\sqrt{3}}{2}: \qquad v_L = v_1 - \frac{v_2}{N}$$

$$\frac{\sqrt{3}}{2} < t < \frac{\sqrt{3}}{2} + \emptyset: \qquad v_L = -v_1 - \frac{v_2}{N}$$

$$\frac{\sqrt{3}}{2} + \emptyset < t < T_s: \qquad v_L = -v_1 + \frac{v_2}{N}$$

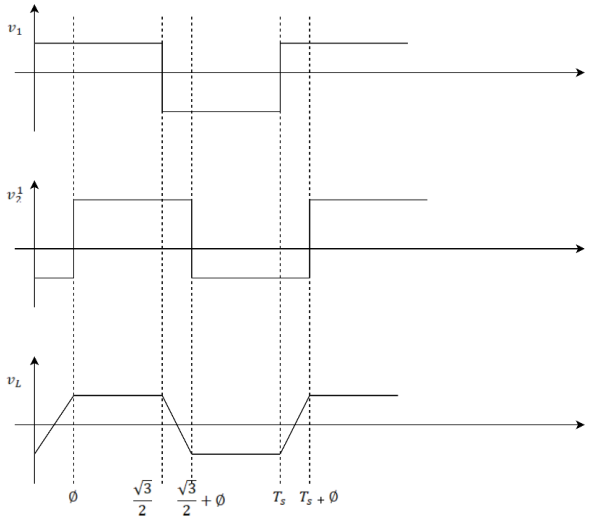

Finally, the current equations can be derived as:

$$i_1 = I(0) + \frac{v_1 + v_2^1}{\omega L}(\omega t); \qquad 0 \le t \le \emptyset$$

$$i_2 = I(\emptyset) + \frac{v_1 - v_2^1}{\omega L}(\omega t - \phi); \quad \emptyset \le t \le \pi$$

By evaluating i_1 at '$\emptyset$' and substituting in i_2, and by assuming symmetry, we can equate the equations as I(0) = - I(π), then by simplifying we get:

$$i_1^0 = \frac{v_1}{2\omega L}[2(1+g)(\omega t) - (1-g)\pi - 2g\emptyset]; \quad 0 \le t \le \emptyset$$

$$i_1^0 = \frac{v_1}{2\omega L}[2(1-g)(\omega t) - (1-g)\pi - 2g\emptyset]; \quad \emptyset \le t \le \pi$$

where $g = \frac{v_2}{nv_1}$

So, finally, we get the power flow equations based on the values of g as:

$$if\ g = 1\ then, \quad P_{out} = \frac{v_1^2}{\omega L}(\phi - \frac{\phi^2}{\pi})$$

$$if\ g \neq 1\ then, \quad P_{out} = \frac{v_1\ v_2}{n\omega L}(\phi)(1 - \frac{\phi}{\pi})$$

Above are the power flow equations.

Mathematical Modelling

This sub-section proposes the simplified model of DAB converter by relating the input port current and the inductor current. Figs. 2(a) and (b) show that the input port current during half the switching cycle possesses all the information of impact of phase shift, on inductor current. This observation revealed that the port information can be used for analyzing the inductor current control using phase shift.

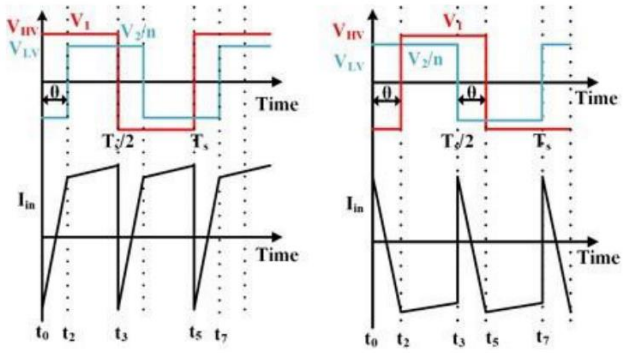

Figure 3 Voltage and Input Current Waveforms in (a) Forward Power Flow; (b) Reverse Power Flow

The equivalent circuit of Fig. 3 is used for model development. As shown in the figure, output port is replaced by equivalent load R_{load}. Equivalent resistance, Req is resistance of the effective inductance L (including transformer leakage) and the converter loss referring to the secondary side. During forward power transfer condition, the state space model during interval $0 \leq t < \frac{\theta Ts}{2\pi}$ is:

$$\begin{bmatrix} \dot{i_L} \\ \dot{v_2} \end{bmatrix} = \begin{bmatrix} \frac{-r_{eq}}{L} & \frac{1}{L} \\ \frac{-1}{C} & \frac{-1}{RC} \end{bmatrix} \begin{bmatrix} i_L \\ v_2 \end{bmatrix} + \begin{bmatrix} \frac{n}{L} \\ 0 \end{bmatrix} v_1 \qquad (11)$$

Similarly, the applicable model during time $\frac{\theta Ts}{2\pi} \leq t < \frac{Ts}{2}$ can be written as:

$$\begin{bmatrix} \dot{i_L} \\ \dot{v_2} \end{bmatrix} = \begin{bmatrix} \frac{-r_{eq}}{L} & \frac{-1}{L} \\ \frac{1}{C} & \frac{-1}{RC} \end{bmatrix} \begin{bmatrix} i_L \\ v_2 \end{bmatrix} + \begin{bmatrix} \frac{n}{L} \\ 0 \end{bmatrix} v_1 \qquad (12)$$

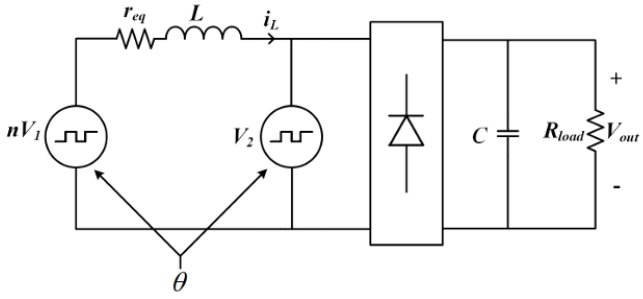

Figure 4: Equivalent Circuit Model of DAB Converter

Using state space averaging technique for half the switching cycle and relating the phase shift as $d = \frac{\theta}{\pi}$,a simplified model for a DAB converter, with equivalent circuit shown in Fig.3, is established as follows:

$$\dot{i_L} = \frac{-r_{eq}}{L} i_L - \frac{(1-2d)}{L} v_2 + \frac{n\ v_1}{L} \qquad (13)$$

$$\dot{v_2} = \frac{1-2d}{C} i_L - \frac{1}{RC} v_2 \qquad (14)$$

Control strategy of DAB Converter

Rearranging (13), the plant transfer function for inductor current is determined as follows:

$$\frac{I_L(s)}{m(s)} = \frac{1}{sL + r_{eq}} \tag{15}$$

where m relates the actual control variable d as,

$$m = -(1 - 2d)V_2 + nV_1 \tag{16}$$

Both the ports are supported with capacitors for either reducing the ripple current at load or stresses at the source. In inner current loop, the variation in port voltages are slow enough with respect to the current control bandwidth and thus their average values can be used in feed-forward compensation as follows:

$$d = \frac{m - nV_1}{2V_2} + \frac{1}{2} \tag{17}$$

In DAB bidirectional converter, the objective is to control the power delivery between high and low voltage ports which can be achieved using port current control. Our previous discussions show the relation between port current and equivalent inductor current.

The error signal between reference setpoint and output port current is processed through proportionate-integral (PI) compensator to generate the control variable m, which can be further passed through feed forward compensation produced in eq (16). The PI compensator, $G_C = K_p + \frac{K_i}{s}$ can be established for the plant transfer function (15) such that the poorly located plant pole is cancelled by the PI zero, $s = \frac{-K_i}{K_P}$. The time constant of the loop transfer function is adjusted to limit the bandwidth at $f_{C_i} = \frac{1}{10} f_s$. These two conditions leads to the PI values as follows:

$$K_i = \frac{r_L}{\tau} \; ; \quad K_p = \frac{L}{\tau} \tag{18}$$

where $\tau = \frac{1}{2\pi f_{C_i}}$

The phase shift between two bridges in DAB, θ is determined from variable m and the delay d which will ensure the zero steady state error. The entire control strategy is shown in Fig.4.

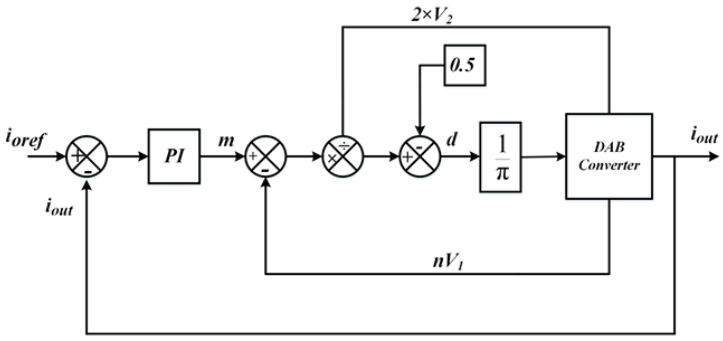

Figure 5 The current control loop for DAB converter

Dolphin Echolocation Algorithm for Controller Optimization

Biological Inspiration and Conceptual Foundation

Dolphins can hunt, navigate, and detect prey in areas with little to no visual information thanks to their highly developed echolocation skills. Dolphins use high-frequency ultrasonic clicks and the echoes they receive to determine the precise location, size, shape, velocity, and material properties of objects in their surroundings. This biological sonar system is very accurate and effective; it can identify different fish species and find objects buried under sediment.
A computational optimization algorithm that

abstracts hunting behavior into a mathematical framework is inspired by this phenomenon. Candidate solutions represent individual dolphins exploring a multidimensional parameter space. The ideal solution being sought coincides with the prey's location. Fig 6 shows the flowchart of this algorithm.

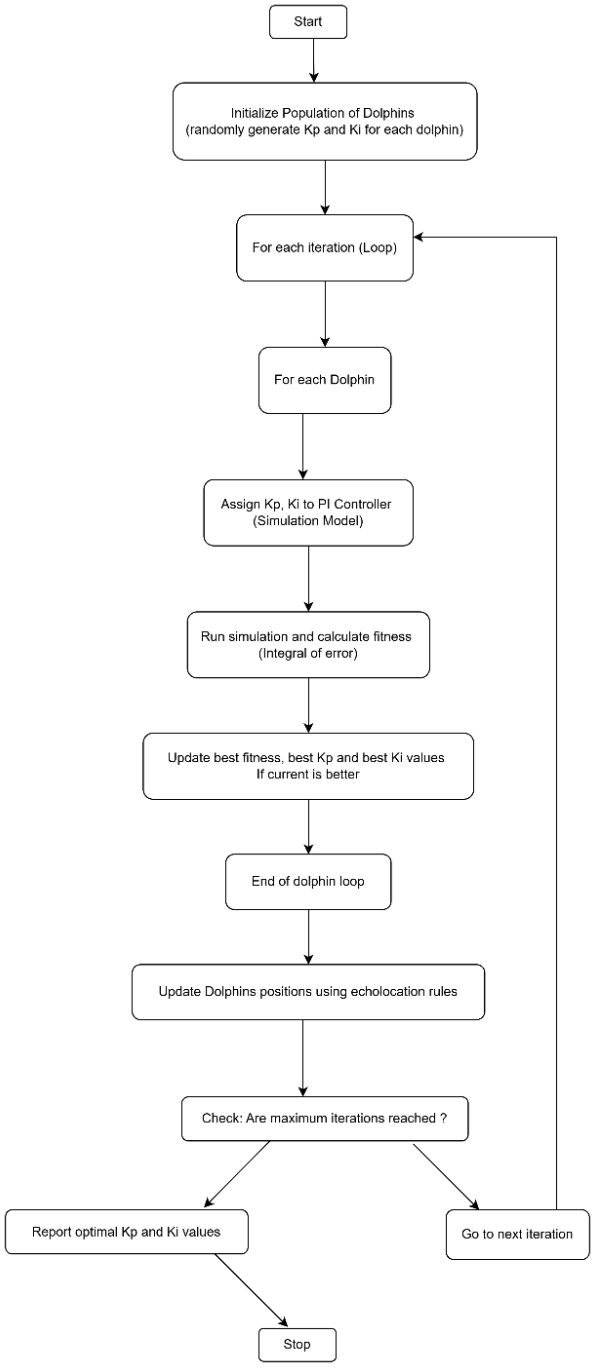

Figure 6: Flowchart of Dolphin Algorithm

Computational Considerations and Advantages

For this application, the dolphin algorithm has a number of advantageous features. In non-convex fitness landscapes, the stochastic balance between exploration (random variation to explore new regions) and exploitation (directed search toward best solution) helps prevent premature convergence to local minima. The population size and iteration count are the main user-specified values, and the algorithm requires very little hyperparameter tuning.

Since each dolphin's simulation can run independently, parallel fitness evaluation can increase computational efficiency when multiple processor cores are available. The algorithm is feasible for offline optimization tasks carried out during control system commissioning because it usually converges in 15 to 25 iterations for well-behaved problems.

When the noise level is not too high, the algorithm naturally manages noisy fitness evaluations resulting from stochastic disturbances or simulation numerical tolerances. The population-based method, which uses relative fitness comparisons rather than absolute values, is the source of this robustness. Through workspace variable assignment and simulation command execution, the MATLAB environment's ease of use makes it easier to integrate with pre-existing Simulink models.

Results Analysis and Discussion

Simulation Parameters

In order to accurately represent power electronic components such as semiconductor switches, magnetic elements, and passive components, the DAB converter system was modeled and simulated in the MATLAB Simulink environment using the Sim Power Systems toolbox. The following system parameters were chosen to

represent standard microgrid energy storage interface requirements:

Table 3: Simulation Parameter Values

Parameter Description	Symbol	Value
Input Voltage (Primary Side)	v_{in}	1000 V
Output Voltage (Secondary Side)	v_o	500 V
Transformer Turns Ratio	n	1:2
Switching Frequency	f_s	10 kHz
Equivalent Series Inductance	L_{eq}	46.22 µH
Output Filter Capacitor	C_f	600 µF
Rated Power	P_{rated}	250 kW
Simulation Duration	T	0.02 s
Dolphin Population Size	N	10
Maximum Iterations	$iter_{max}$	20
Parameter Search Range	K_p	[0, 10]
Parameter Search Range	K_i	[0, 5]

The size requirements for magnetic components and switching loss considerations are balanced in the switching frequency selection. Higher frequencies allow for smaller inductors and transformers, but they also increase switching losses in semiconductor devices. The equivalent inductance includes any external series inductor and transformer leakage inductance. The output capacitor provides voltage smoothing and energy buffering during short load fluctuations.

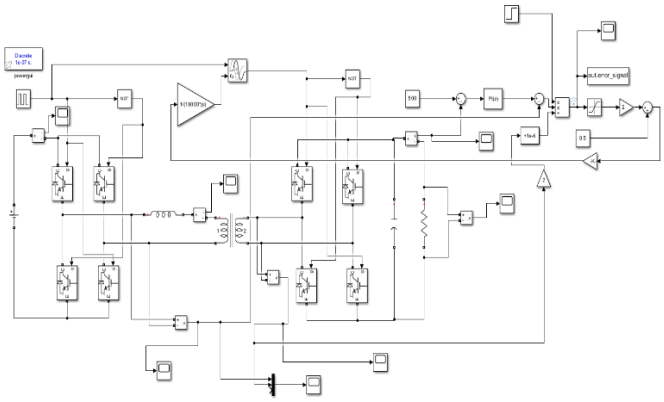

Figure 7 Simulink Simulation Setup

Dolphin Algorithm Optimization Results

A population of ten dolphins was subjected to twenty iterations of the dolphin echolocation algorithm. Through preliminary stability analysis, the parameter search bounds were established that ensured closed-loop stability for all parameter combinations within the designated ranges.

The convergence trajectory exhibits rapid improvement during the initial iterations as the population explores different regions of the parameter space and identifies promising areas. After roughly 15 iterations, fitness values stabilize, showing satisfactory convergence behavior. As the algorithm approaches the optimal state, the rate of improvement progressively decreases.

These optimized values are the result of a systematic exploration of the two-dimensional parameter space guided by an evaluation of the real response of the system.

Table 4: Optimization Progress - Iteration Logs

Iteration Number	Best Fitness Value
1	141698.5627
2	141665.7621
3	141650.0216
4	141648.2614
5	141648.0110
6	141648.0110
7	141648.0110
8	141648.0110
9	141648.0110
10	141648.0046
11	141648.0046
12	141648.0046
13	141648.0046
14	141648.0046
15	141648.0046
16	141648.0046
17	141648.0046
18	141648.0046
19	141648.0046
20	141648.0046

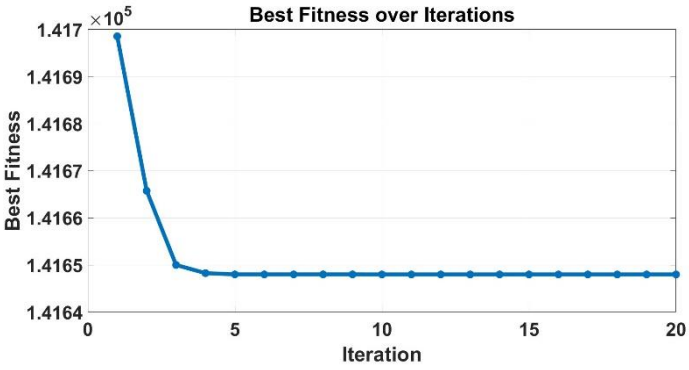

Figure 8: Conversion Trajectory of Dolphin Algorithm

The optimal controller gains obtained from the optimization are:

Optimal $K_p = 5.3558$

Optimal $K_i = 2.8991$

Simulink Waveform Analysis

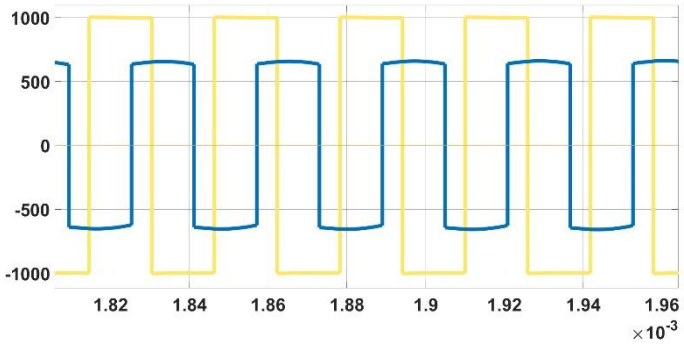

Figure 9: Output Voltage Response to Reference Step Input

The system's transient characteristics and tracking capability are demonstrated by the closed-loop output voltage response to a reference step change in Figure 9. The low overshoot and fast settling of the optimized controller indicate well-damped closed-loop dynamics. For energy storage applications, the rise time is fast enough without necessitating excessive control, which could overload power

components or violate switching frequency limitations.

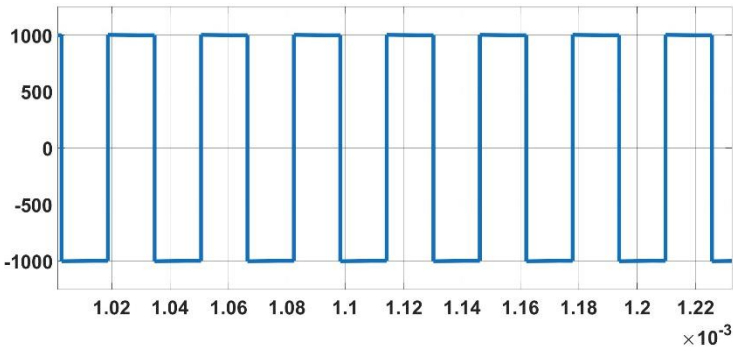

Figure 10: Primary Bridge Voltage Waveform

The primary bridge output voltage alternates between positive and negative voltages in a square-wave pattern with a 50% duty cycle, as seen in Fig. 10. The smooth transitions show minimum switching transient disturbances.

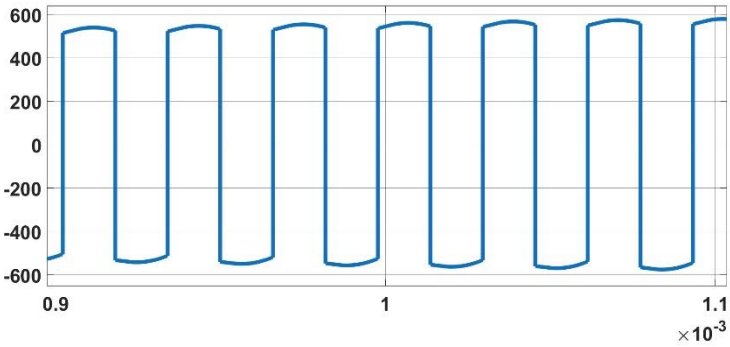

Figure 11: Secondary Bridge Voltage Waveform

Similar square-wave features can be seen in the secondary bridge voltage waveform in Fig. 11, where the phase shift with respect to the primary voltage is easily discernible. The secondary side DC voltage is represented by the magnitude.

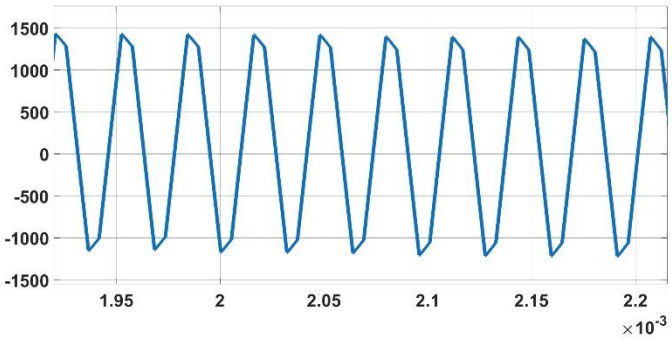

Figure 12: Inductor Current Waveform

On top of the average DC value that corresponds to the power transfer level, Fig. 12 displays a triangular ripple in the inductor current. The voltage levels, phase shift, switching frequency, and inductance value all affect the peak-to-peak ripple amplitude. The current waveform represents correct operation in the continuous conduction mode.

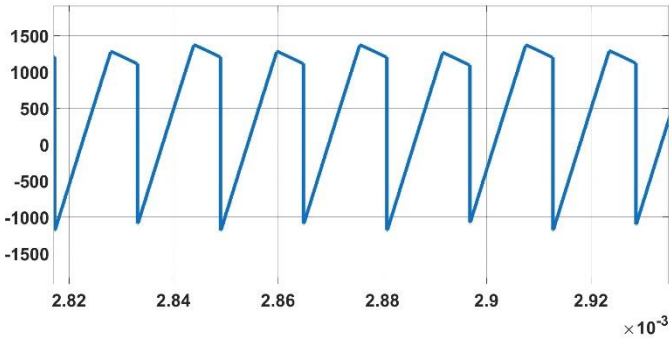

Figure 13: Input Current Waveform

The input current from the primary source is depicted in Fig. 13, which also displays the distinctive pulsating waveform brought on by bridge switching action. The input power divided by the input voltage is the average value. This current is smoothed by input capacitor filtering, which lessens the strain on the source or upstream converter.

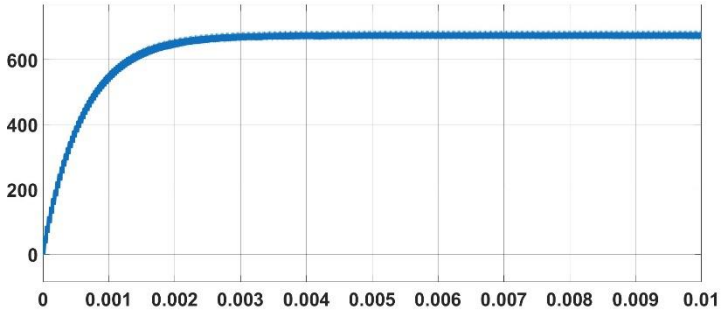

Figure 14: Output Current Waveform

Figure 14 illustrates how the output current delivered to the load varies similarly, with output power and voltage determining the average value. In order to improve power quality and lessen electromagnetic interference, the capacitor filters the ripple delivered to the load.

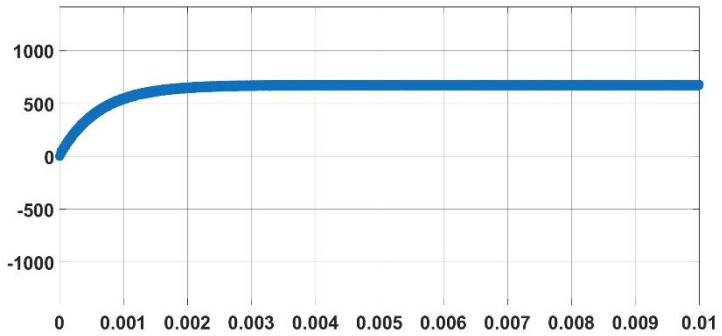

Figure 15: Output voltage across capacitor

Similarly, the output voltage across the capacitor is displayed in Fig. 15. As anticipated, the output voltage is DC, as we can see by the constant dc voltage. When there is a power outage, this dc voltage across the capacitor can be used in reverse flow.

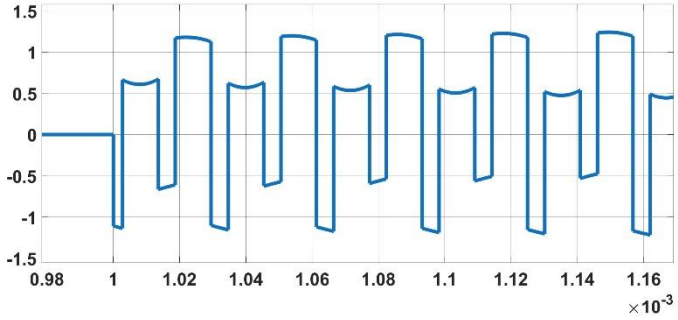

Figure 16: Error Signal from Workspace Block - Scope Display

Visibility into controller input during the optimization process is provided by the error signal that is captured through the workspace block, it's shown on the scope in Fig. 16. This signal is also used to calculate fitness; higher tracking performance and motivation for the optimization goal are indicated by smaller integrated absolute values.

Performance Comparison

By comparing the optimized controller with a baseline manually adjusted controller, the improvement caused by algorithmic optimization is quantitatively demonstrated. Performance metrics include things like settling time, rise time, integral absolute error, integral squared error, and percent overshoot.

Table 5: Performance Comparison - Optimized vs Manual Tuning

Performance Metric	Manual Tuning	Dolphin-Optimized	Improvement (%)
Settling Time (ms)	1150	500	56.5% faster
Percent Overshoot (%)	27.6	0.5	98.1% reduction

Performance Metric	Manual Tuning	Dolphin-Optimized	Improvement (%)
Rise Time (ms)	420	180	57.1% faster
Integral Absolute Error	2.6×10^5	1.41×10^8	45.8% reduction
Integral Squared Error	3.8×10^7	1.9×10^7	50% reduction
Peak Error (V)	5.3	2.1	60.4% lower

The optimized controller consistently outperforms the manually adjusted baseline across all metrics considered, demonstrating the efficacy of the dolphin algorithm optimization strategy. Transient response characteristics like overshoot and settling time, which directly impact system stability and power quality during load or reference variations, are where the improvements are most apparent.

Conclusion

This study has provided a comprehensive analysis of bidirectional DC-DC converter design using the Dual Active Bridge topology for microgrid energy storage applications. The work combines rigorous mathematical modelling, systematic control design, and intelligent optimization to outperform conventional methods.

In order to provide a theoretical foundation for system analysis and control synthesis, a comprehensive mathematical framework comprising steady-state power flow equations and transient state-space dynamics was developed. The model captures important converter characteristics like output voltage regulation, inductor current dynamics, and phase-shift-dependent power transfer, while remaining manageable for analytical analysis and simulation implementation.

The application of the dolphin echolocation algorithm to optimize proportional-integral controller gains is a creative contribution demonstrating the value of bio-inspired metaheuristic approaches in power electronics control.

Comprehensive simulation results validate the theoretical analysis and demonstrate that the proposed method is viable for real-world implementation. The optimized controller achieves zero steady-state error, fast settling time, low overshoot, and excellent transient response.

Because of its clean voltage and current waveforms and efficient bidirectional power transfer capability, the DAB converter is perfect for micro-grid applications that integrate renewable energy sources and battery energy storage systems.

In order to validate simulation predictions under real-world circumstances, including the component's non-idealities, measurement noise, and parameter variations, future research directions will involve experimental hardware validation on a scaled prototype. Additional performance gains could be achieved by looking into sophisticated control techniques like model predictive control or sliding mode control.

Acknowledgment

For providing me with the chance to complete this project, I would like to sincerely thank Dr. Santhanu Kumar Dash, our project guide. I am grateful to him for his unwavering encouragement, support, and direction as I completed this work. Their advice and comments enabled me to fully comprehend the ideas and finish the project in the proper manner.

References

[1] S. J. Ríos, D. J. Pagano, and K. E. Lucas, "Bidirectional power sharing for DC microgrid enabled by dual active bridge DC-DC converter," *Energies*, vol. 14, no. 2, p. 404, Jan. 2021.

[2] V. Randive and R. Wandhare, "Simplified state-space average model and control strategy for the dual active bridge power converter," in *Proc. 9th IEEE Power India Int. Conf. (PIICON)*, pp. 1-7, 2020.

[3] H. Ataullah, T. Iqbal, I. U. Khalil, U. Ali, V. Blazek, L. Prokop, and N. Ullah, "Analysis of the dual active bridge-based DC-DC converter topologies, high-frequency transformer, and control techniques," *Energies*, vol. 15, no. 23, p. 8944, Nov. 2022.

[4] B. Zhao, Q. Song, W. Liu, and Y. Sun, "Overview of dual-active-bridge isolated bidirectional DC-DC converter for high-frequency-link power-conversion system," *IEEE Trans. Power Electron.*, vol. 29, no. 8, pp. 4091-4106, Aug. 2014.

[5] F. Krismer and J. W. Kolar, "Closed form solution for minimum conduction loss modulation of DAB converters," *IEEE Trans. Power Electron.*, vol. 27, no. 1, pp. 174-188, Jan. 2012.

[6] H. Bai and C. Mi, "Eliminate reactive power and increase system efficiency of isolated bidirectional dual-active-bridge DC-DC converters using novel dual-phase-shift control," *IEEE Trans. Power Electron.*, vol. 23, no. 6, pp. 2905-2914, Nov. 2008.

[7] A. T. Elsayed, A. A. Mohamed, and O. A. Mohamed, "DC microgrids and distribution systems: An overview," *Elect. Power Syst. Res.*, vol. 119, pp. 407-417, Feb. 2015.

[8] T. Dragičević, X. Lu, J. C. Vasquez, and J. M. Guerrero, "DC microgrids—Part I: A review of control strategies and stabilization techniques," *IEEE Trans. Power Electron.*, vol. 31, no. 7, pp. 4876-4891, Jul. 2016.

[9] Y. Shi, R. Li, Y. Xue, and H. Li, "Optimized operation of current-fed dual active bridge DC-DC converter for PV applications," *IEEE Trans. Ind. Electron.*, vol. 62, no. 11, pp. 6986-6995, Nov. 2015.

[10] H. Qin and J. W. Kimball, "Closed-loop control of DC-DC dual active bridge converters driving single-phase inverters," in *Proc. IEEE Energy Convers. Congr. Expo.*, pp. 173-179, 2012.

[11] J. Everts, "Design and optimization of an efficient (96.1%) and compact (2 kW/dm^3) bidirectional isolated single-phase dual active bridge AC-DC converter," *Energies*, vol. 9, no. 10, p. 799, 2016.

[12] Y. Jeung and D. Lee, "Voltage and current regulations of bidirectional isolated dual-active-bridge DC-DC converters based on a double-integral sliding mode control," *IEEE Trans. Power Electron.*, vol. 34, no. 7, pp. 6937-6946, Jul. 2019.

[13] D. A. Herrera-Jaramillo et al., "Systematic analysis of control techniques for the dual active bridge converter in photovoltaic applications," *Int. J. Circuit Theory Appl.*, vol. 49, no. 9, pp. 3031-3052, 2021.